

Drag Reduction by Surface Actuation



Marian Albers, Matthias Meinke, and Wolfgang Schröder

Abstract The flow over an DRA2303 wing section is controlled by spanwise traveling transversal surface waves. The actuated flow field is investigated by large-eddy simulation. Approximately 74% of the solid surface is deflected by a sinusoidal space- and time-dependent function in the wall-normal direction. Viscous drag reduction by 8.6% with a strong decrease of skin-friction in the favorable pressure gradient region and an overall drag decrease by 7.5% are achieved. Furthermore, a slight increase in lift is obtained for the external flow over a realistic geometry.

1 Introduction

Despite more efficient aircraft engines, the interest in reducing friction drag, which makes up to 50% of the total drag for standard narrow- and wide-body aircraft, is still high. A large variety of approaches has already been considered in the literature.

In general, the drag reduction techniques can be categorized in active or passive methods. Among passive methods, longitudinal grooves aligned with the streamwise direction, so-called shark-skin surfaces or riblets are well known. Early works by Walsh and Weinstein [55] and Bechert et al. [6] proved the general applicability of ribbed surfaces to lower turbulent friction drag. The responsible mechanism was shown in [24] to be related to the imposition of the no-slip condition for the spanwise velocity fluctuations at greater height into the flow than for the streamwise and wall-normal velocity components, thereby driving quasi-streamwise vortices further off the wall. García-Mayoral and Jiménez [16] investigated the degradation of the drag reduction at increasing riblet sizes and showed the link to a two-dimensional Kelvin-Helmholtz-like instability of the mean streamwise flow. In-flight tests confirmed the drag reducing effect using an aircraft partially covered with riblets [49]. However,

M. Albers (✉) · M. Meinke · W. Schröder
Institute of Aerodynamics, RWTH Aachen University, Wüllnerstrasse 5a, 52062 Aachen,
Germany
e-mail: m.albers@aia.rwth-aachen.de

W. Schröder
JARA – High-Performance Computing, Forschungszentrum Jülich, 52425 Jülich, Germany

© Springer Nature Switzerland AG 2021

W. E. Nagel et al. (eds.), *High Performance Computing in Science and Engineering '19*,
https://doi.org/10.1007/978-3-030-66792-4_20

the sensitivity of the drag reducing effect of riblets to surface deterioration due to long-term use and the challenge to ensure the optimal riblet size to varying flow conditions have prevented their application in a production environment [43]. Besides riblets, other passive approaches are available. The use of compliant surfaces seems to be promising [10, 28, 34, 56]. The injection of gas reduces drag [9, 40]. Moreover, superhydrophobic surfaces yield interesting findings in turbulent flows [18]. Extensive research on large-eddy breakup devices showed hardly any energy saving in practical applications [3]. Other methods achieve drag reduction by stabilizing the wake in the downstream region of the airfoil [7].

A solution to the small-parameter-range drawback of passive methods can be overcome by active methods. They offer the possibility to alter the actuation parameters based on the operating conditions. The maximum drag reduction rates of most methods are higher than those of passive techniques. Following the observation of suppressed turbulent production by temporal spanwise pressure gradients [38], Jung et al. [26] measured turbulent flow with spanwise wall oscillations. In turbulent channel flows, they achieved drag reduction rates up to 40%.

Ever since, a wide variety of actuation types has numerically and experimentally been developed and tested. An excellent review on the different approaches is given by Quadrio [41]. Streamwise traveling waves of spanwise wall velocity were applied to turbulent channel flow by Quadrio et al. [42], yielding up to 60% drag reduction. Nakanishi et al. [39] investigated waves of wall-normal motions traveling in the streamwise direction determined relaminarized flow. A wave-like wall-normal excitation of piezo-actuator array decreased the wall-shear stress locally and a quick recovery was observed in [5]. Another promising approach is a forcing by spatial waves in the spanwise direction investigated by Du and Karniadakis [11] and Du et al. [12]. They found considerable reduction of the turbulent streamwise intensities, resulting in a reduced overall skin friction. Zhao et al. [57] advanced the idea by deriving an equivalent in-plane velocity. A similar type of control in turbulent boundary layer flow was conducted by Itoh et al. [22] and Tamano and Itoh [50]. The skin-friction was reduced by up to 13%. Numerical investigations by Klumpp et al. [30] and Koh et al. [31] confirmed these findings for a long wavelength, while a shorter wavelength enlarged the drag. The extension of these investigations to non-zero pressure gradient turbulent boundary layers [36] revealed a decreased drag reduction rate. More recent results [1] indicate a higher drag reduction potential for smaller wave periods and larger wavelengths.

The majority of the former research focuses on canonical flow problems, whereas only some investigations consider engineering-like flow geometries. Active modifications of the attached turbulent boundary layer on wing surfaces are primarily based on blowing and/or suction [33]. This, however, can result in increased boundary-layer thicknesses and more energetic fluctuations [27, 52]. Recent results by Atzori et al. [4] show promising reductions of the skin friction.

Combined passive and active measures are often considered in laminar flow control (LFC) [43], either by modifying the airfoil shape, natural laminar flow (NLF), or by an additional active technique, hybrid laminar flow control (HLFC), to control the development of instabilities [15]. HLFC has been tested in flight [19] and is currently

applied to the Boeing 787-9. Note that the skin-friction is increased in the remaining turbulent boundary layer due to the lower thickness Reynolds number compared to the non-controlled case [47].

In brief, there is an enormous amount of literature on drag reduction available. However, hardly any of the active turbulent control approaches have been analyzed for more realistic configurations. The techniques which have been used in realistic flow setups do not directly interact with the turbulent flow field or possess technical difficulties. For this reason, the active drag reduction technique based on spanwise traveling transversal surface waves [36], will be applied to the wing section of an DRA2303 airfoil. It is the objective to reduce the overall drag for such an engineering geometry without an increase of the pressure drag and without lowering the lift. The full analysis of the drag reduction potential is published in [2]. This contribution represents a concise excerpt of the aforementioned paper.

2 Numerical Method

The computational approach is based on a finite volume approximation of the Navier-Stokes equations for unsteady compressible flows. The large-eddy simulation (LES) concept is used to determine the turbulent flow field. A second-order accurate formulation of the convective fluxes using the Advection Upstream Splitting Method (AUSM) [32] is applied. The viscous fluxes are discretized by a modified cell-vertex scheme [35]. The time integration is performed by a second-order accurate 5-stage Runge–Kutta scheme. The smallest turbulent scales are modeled by the monotonically integrated large-eddy simulation (MILES) approach [8]. A detailed discussion of the method and the subgrid-scale model was presented in [35]. To capture the wall motion, the Arbitrary Lagrangian–Eulerian (ALE) formulation of the Navier-Stokes equations is used [20].

A parallelization with distributed memory and communication via the message passing interface (MPI) is employed. The structured mesh is partitioned using a tree-based splitting algorithm to generate sub-blocks of the global mesh [17]. Each sub-block is assigned to one parallel process and the flow variables at the sub-block interfaces are exchanged in every Runge–Kutta sub-step.

This numerical method has thoroughly been extensively validated, see e.g. [29, 30, 37, 44].

3 Computational Setup

The flow is defined in a Cartesian domain around an infinite wing section with the x -axis being the airfoil chord, the z -axis defining the direction of the infinite wing span, and the y -axis being perpendicular to the other two axes. Positions are $\mathbf{x} = (x, y, z)$ and velocities are denoted by $\mathbf{u} = (u, v, w)$, the pressure is given by p and the density

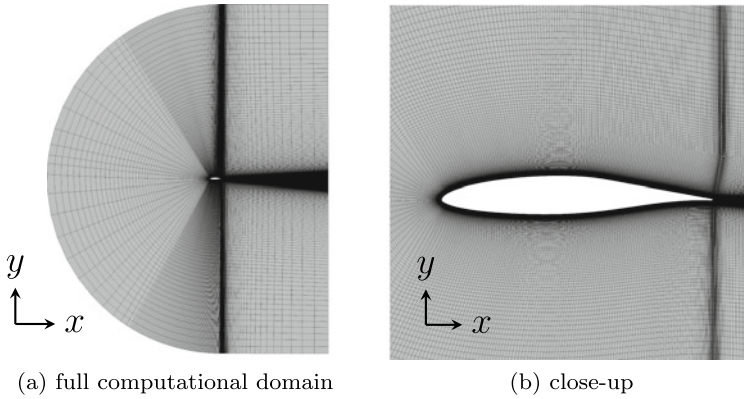


Fig. 1 C-type body-fitted mesh; the x -axis is aligned with the airfoil chord, only every 10th grid point in the wall-tangential direction is shown; **a** full computational domain; **b** close-up view

by ρ . The geometry of the wing section is defined by an DRA2303 airfoil with a maximum thickness of 14% chord. The flow field of this supercritical laminar-type airfoil has extensively been investigated for transonic flows [13, 14, 44, 48]. It can be considered a fundamental generic airfoil for this flow regime [31, 37]. The minimum of the pressure coefficient $c_{p,min} = \min((p - p_\infty)/(\rho_\infty u_\infty^2))$ on the suction side of the airfoil is reached almost at mid-chord, i.e., $(x/c)_{c_{p,min}} \approx 0.5 - 0.55$.

A block-structured three-dimensional body-fitted C-type mesh is used to discretize the physical domain with an extension of 15 chord lengths upstream and 10 chord lengths downstream of the wing. The size of the computational domain is substantially larger than in the DNS by Shan et al. [46]. In the spanwise direction, the wing section is 10% chord wide. This width suffices to capture at least three boundary layer thicknesses and is wide enough to consider multiple wave lengths of the actuation function. A two-dimensional representation of the numerical domain is shown in Fig. 1a with a close-up of the mesh in the vicinity of the airfoil shown in Fig. 1b.

A RANS simulation of the same setup with a larger domain size of $L_x \times L_y = 120c \times 120c$ yielded the same pressure distribution. The grid resolution in inner scaling on the wing surface near the leading and the trailing edge is $\Delta x^+ < 21.0$, $\Delta y^+ < 1.3$, and $\Delta z^+ < 8.0$. The final grid consists of 408 million cells.

No-slip solid wall boundary conditions are imposed on the surface of the airfoil. Characteristic inflow conditions are defined on the far-field boundaries on the left and lower boundary and characteristic outflow conditions including the ambient pressure p_∞ are used on the upper and right boundary. An additional sponge suppresses the reflection of outgoing pressure waves at the boundaries. In the spanwise direction, periodic boundary conditions are applied.

A numerical tripping at $x/c = 0.1$ on both sides of the airfoil triggers laminar-turbulent transition [21, 45].

The freestream Mach number is $M = 0.2$ and the angle of attack is $\alpha = 2.0$. The chord of the airfoil is aligned with the x -axis. The freestream Reynolds number based on the chord length of the airfoil is $Re = 400,000$, i.e., comparable to [21]. This problem can still be computed in an acceptable time frame. The traveling wave of the surface is given by

$$y_n^+|_{\text{wall}}(z^+, t^+) = A^+ \cos\left(\frac{2\pi}{\lambda^+} z^+ - \frac{2\pi}{T^+} t^+\right) . \quad (1)$$

The quantity $\lambda^+ = \lambda u_\tau / \nu$ is the wavelength, $A^+ = A u_\tau / \nu$ the amplitude, and $T^+ = T u_\tau^2 / \nu$ the period in inner scaling. A smooth transition from the non-actuated to the actuated surface and vice versa is guaranteed by a $1 - \cos(x)$ function in the streamwise intervals $0.2 \leq x/c \leq 0.25$ and $0.9 \leq x/c \leq 0.95$. In terms of the chordwise coordinate system 74.02% of the integrated wetted surface undergo an actuation. The limits of the actuated area ensure that a large percentage of the airfoil surface is influenced by the sinusoidal wall motion. Note that the temporal transition from the non-actuated to the actuated surface is also described by a $1 - \cos(t)$ function. The values of the parameters of the wave motion are based on results of previous analyses of zero-pressure gradient turbulent boundary layer flows [1, 30, 31, 37]. Using the previous findings, the amplitude is prescribed in the range $30 \leq A^+ \leq 50$. To keep the increase of the wetted surface due to the wall deflection small, a long wavelength is preferred. The most promising period of the actuation function is found to be in the range $30 \leq T^+ \leq 50$ [1, 30]. Due to the variation of the friction velocity u_τ in the streamwise coordinate x , the wave parameters are a function of the x -direction to approximate the optimal range in most parts of the wing. The amplitude varies in the streamwise direction. This is especially relevant in the adverse-pressure-gradient region, i.e., $x/c > 0.55$, to balance the reduced drag reduction potential due to the positive pressure gradient conditions [36].

The characteristic time scale of the large scales based on u_τ and δ_0 at $x/c = 0.8$ on the suction side is similar to that in [54] for a comparable setup. Note that no normalized eddy-turnover time [53] is given since no homogeneous direction exists for the actuated setup. The instantaneous solution of the non-actuated flow is used as initial distribution for the actuated flow. Again, when the steady state of the lift and drag coefficient of the actuated case is reached the computation is performed for another five flow-over times to sample enough data for the turbulence statistics. For the non-actuated flow, the solution fields are spanwise averaged and for the actuated case phase averaged.

4 Computing Resources

The computation of the actuated airfoil flow problem requires a high amount of computational resources. This is mainly due to the relatively high Reynolds number of $Re_c = 400,000$ and the requirements of the wall-resolved large-eddy simulation

(LES) approach. That is, most of the turbulent scales need to be resolved and a high mesh resolution is required, especially in the near-wall region and in the wake flow. The final mesh consists of 408 million cells and is furthermore time-dependent. Thus, in addition to the numerical flux discretization the geometrical properties, i.e., the metric terms, need to be recalculated in every Runge–Kutta sub-time step. Besides, to guarantee a stable and conservative solution the geometry conservation law (GCL) needs to be fulfilled, requiring the computation of the additional volume flux. The simulation was carried out on 200 compute nodes of the high-performance platform Hazelhen, where each node consists of two Intel® Xeon® E5-2680 v3 CPUs, i.e., a total of 4,800 cores were used. On average, each partition contains approximately 85,000 cells and one core is used for each partition. The total run time of one simulation was $2.5 \cdot 10^6$ iteration steps translating into 524 h of actual computation time and a total of $2.51 \cdot 10^6$ core hours required.

5 Results

In Fig. 2, the flow field over the actuated wing section is shown by contours of the λ_2 -criterion [23] colored by the streamwise velocity component. The flow is tripped at $x/c = 0.1$ and the transition from the non-actuated to the actuated surface is imposed at $x/c = 0.2$. The turbulent structures in the outer boundary layer cover the changes in the near-wall structures that are responsible for the differences in the wall-shear stress of the actuated and the non-actuated flow.

The temporal evolutions of the combined viscous and pressure drag

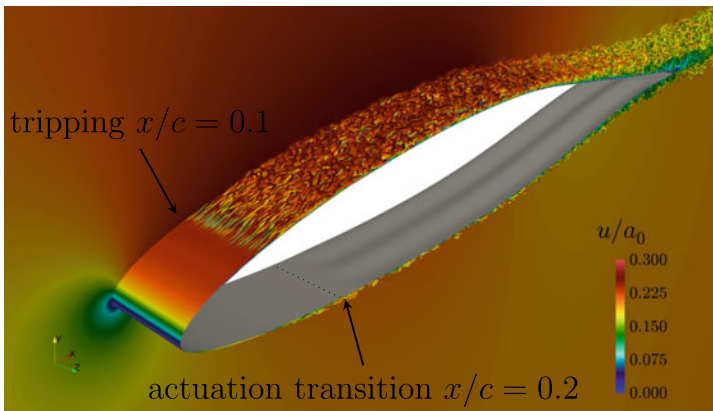


Fig. 2 Contours of the λ_2 -criterion above the actuated airfoil, colored by the streamwise velocity component

$$c_d = \frac{2}{\rho_\infty u_\infty^2 A_{ref}} \left(\int_A \tau_w(\mathbf{n} \cdot \mathbf{e}_y) dA - \int_A p(\mathbf{n} \cdot \mathbf{e}_x) dA \right),$$

the viscous drag in the x -direction

$$c_{d,v} = \frac{2}{\rho_\infty u_\infty^2 A_{ref}} \int_A \tau_w(\mathbf{n} \cdot \mathbf{e}_y) dA,$$

and the lift in the y -direction

$$c_l = \frac{2}{\rho_\infty u_\infty^2 A_{ref}} \left(\int_A \tau_w(\mathbf{n} \cdot \mathbf{e}_x) dA - \int_A p(\mathbf{n} \cdot \mathbf{e}_y) dA \right),$$

are presented in Fig. 3. The wall-shear stress and the pressure are integrated over the whole surface of the wing section. To emphasize the differences between the actuated and the non-actuated flow the distributions are scaled by the mean coefficients of the non-actuated reference case $\bar{c}_{d,ref}$, $\bar{c}_{d,v,ref}$, and $\bar{c}_{l,ref}$. During the temporal transition from the non-actuated to the actuated flow, the total drag of the actuated case starts to reduce and reaches a new quasi-steady state after about 0.25 flow-over times. A similar behavior is observed for the viscous drag coefficient in Fig. 3b. The temporal evolution of the lift coefficient in Fig. 3c shows a larger delay with a visible increase only after about 0.7 flow-over times. On average, a decrease of the total drag by 7.5% is achieved and the lift coefficient is even slightly increased by 1.4%. The large wavelength results in only a minor increase of the wetted surface by 1.6% such that the viscous drag coefficient is reduced by 8.6%.

The mean wall-tangential velocity distributions in the wall-normal direction at the streamwise positions $x/c = 0.5$ and $x/c = 0.7$ on the suction and the pressure side of the wing section are depicted in Fig. 4. The position $x/c = 0.5$ is located in the zero pressure gradient region and the location $x/c = 0.7$ in the adverse pressure gradient region in the aft part of the wing section. Note that the velocities are normalized by the friction velocity of the non-actuated reference case to enable a direct comparison. At all four locations, the velocity distribution in the trough region of the phase-averaged wave is significantly lowered, whereas only slight variations are observed in the near-wall region on the wave crest. This behavior is consistent with previous investigations of transversal surface waves on zero-pressure gradient turbulent boundary layers, where the essential drag reduction is achieved in the trough region of the wave [31]. In the following, we will focus on the two locations, i.e., $x/c = 0.5$ and $x/c = 0.7$, on the upper side.

A detailed look of the impact of the wave motion on the turbulent field is taken in Fig. 5, where the normal components of the Reynolds stress tensor in the wall-tangential, wall-normal, and spanwise direction are shown at the two positions on the suction side. The distributions of the shear-stress component are also illustrated. The fluctuations in the 4a direction in Fig. 4a, b are clearly reduced in the crest and the trough region. Due to the zero pressure gradient and the higher wave amplitude in inner units, the decrease of the fluctuations is stronger at the upstream position.

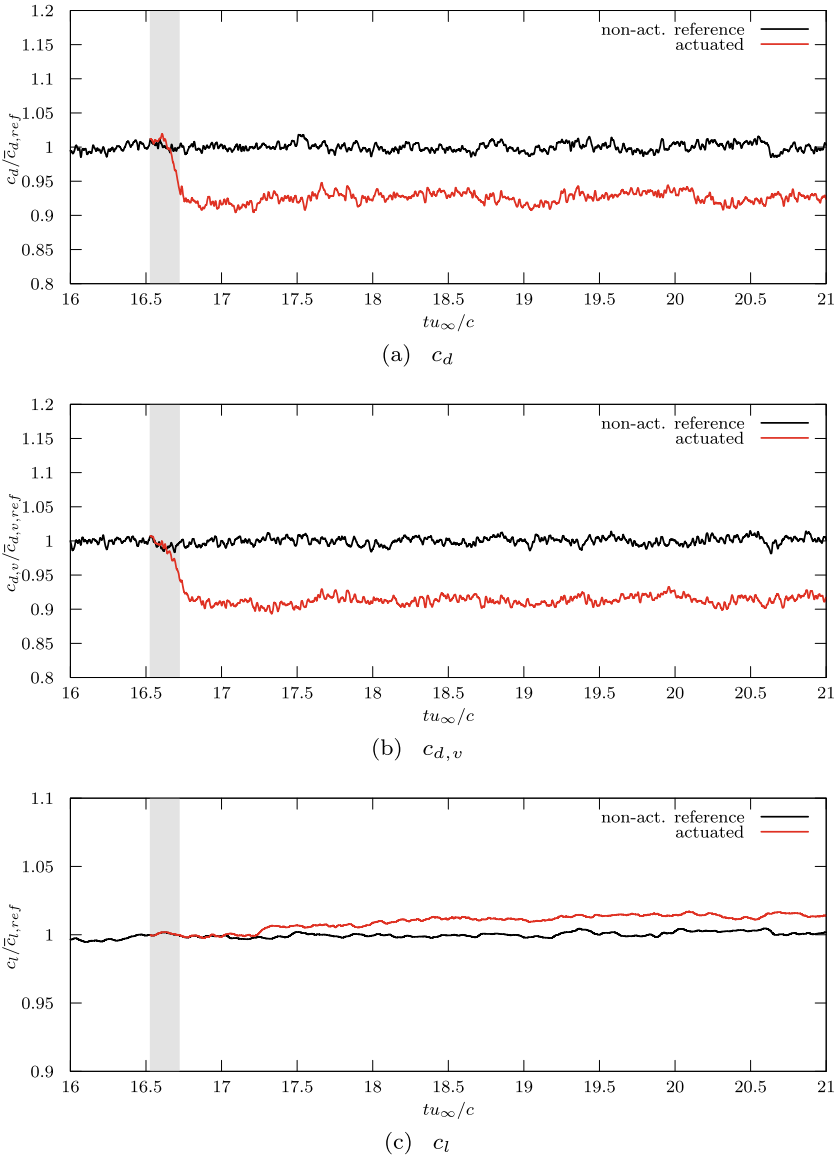


Fig. 3 Temporal evolution of **a** the ratio of the instantaneous total drag coefficient of the actuated case to the averaged drag coefficient of the non-actuated reference case, **b** the ratio of the instantaneous viscous drag coefficient of the actuated case to the averaged viscous drag coefficient of the non-actuated reference case, and **c** the ratio of the instantaneous lift coefficient of the actuated case to the averaged lift coefficient of the non-actuated reference case; the grey column indicates the time of the temporal transition from non-actuated to the actuated case

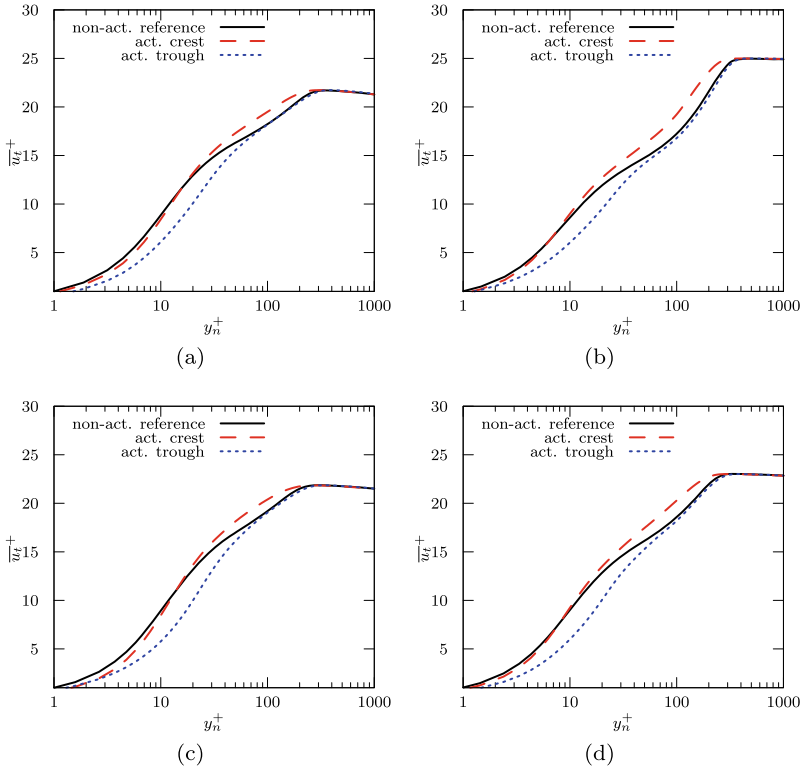


Fig. 4 Averaged wall-tangential velocity component distribution at $x/c = 0.5$ (left column) and $x/c = 0.7$ (right column) on the suction side (top) and on the pressure side (bottom) of the wing section for the non-actuated reference and the actuated case

In the wave trough, a shift of the peak of the fluctuations off the wall is apparent. This is caused by shielding the wall from quasi-streamwise vortices [31, 51]. While the fluctuations in the wall-normal direction in Fig. 4c, d are significantly decreased at the upstream position, they remain almost unchanged in the adverse pressure gradient region at $x/c = 0.7$. For the spanwise fluctuations in Fig. 4e, f the result is more diverse. An apparent decrease occurs in the zero pressure gradient region and an increase in the adverse pressure gradient region. In general, the zero pressure gradient conditions are beneficial for the wave motion, supporting the reduction of turbulent motion near the wall, whereas the adverse pressure gradient counteracts the desired effect of the actuation for the current set of wave parameters. The positive pressure gradient causes a lower wall-shear stress already in the non-actuated flow. This means that a reduced actuation, i.e., a smaller amplitude, is more efficient than the current surface motion [36].

Finally, the wall-tangential and the wall-normal vorticity fluctuations are considered. Jiménez and Pinelli [25] showed that a suppression of wall-normal vorticity

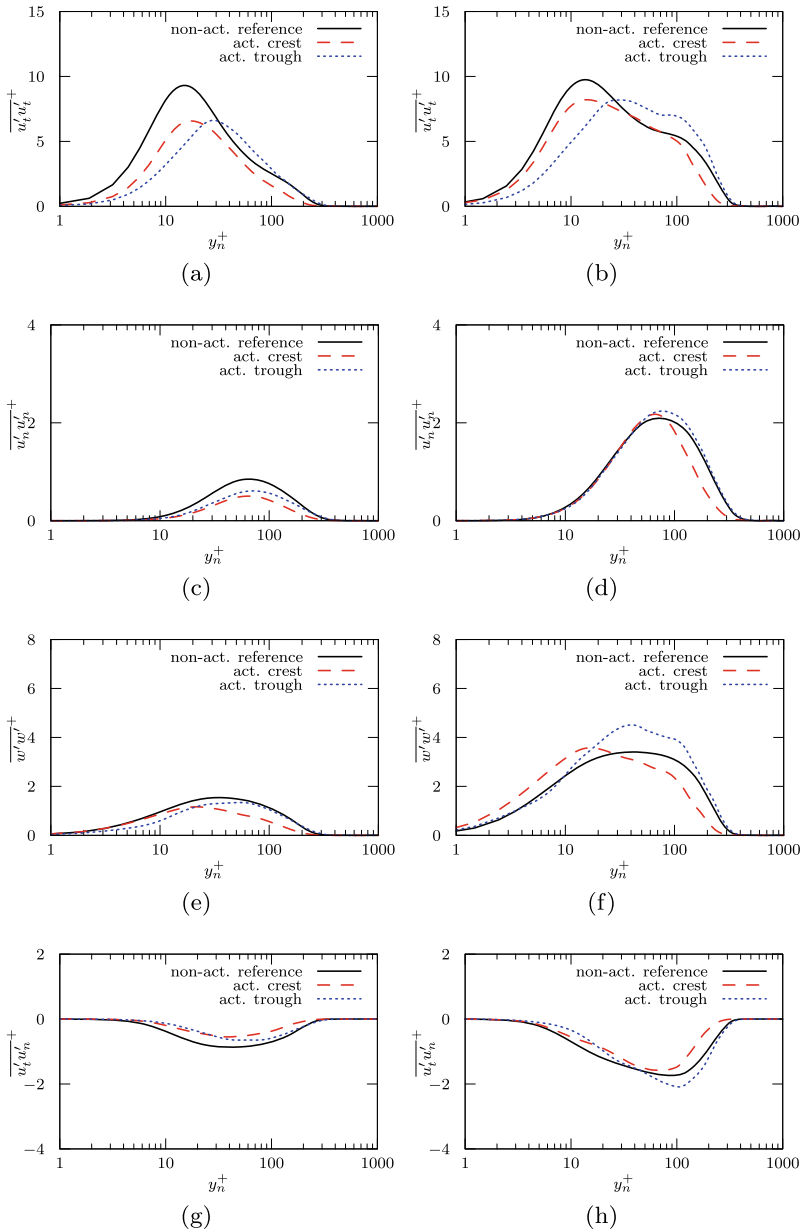


Fig. 5 Averaged distributions of the Reynolds stress tensor components at $x/c = 0.5$ (left column) and $x/c = 0.7$ (right column) on the suction side of the wing section

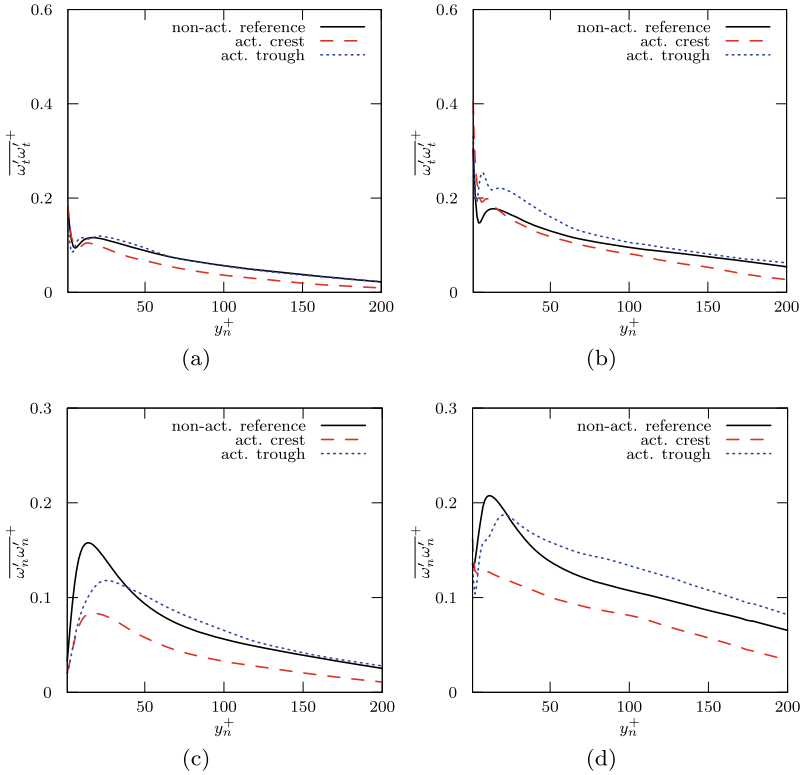


Fig. 6 Distribution of the root-mean-square of the vorticity fluctuations in inner units at $x/c = 0.5$ (left column) and $x/c = 0.7$ (right column) on the suction side of the wing section for the non-actuated reference and the actuated case; **a, b** wall-tangential vorticity component; **c, d** wall-normal vorticity component

fluctuations can be directly related to a decrease of the turbulent velocity fluctuations and thus to a decrease of the skin friction. This has been confirmed in [30] for an actuated flat plate flow and a similar conclusion can be drawn from Fig. 6. The decrease of the wall-normal component is observed in the near-wall region at both positions, with a stronger reduction in the zero pressure gradient region and generally on the wave crest. The distributions of the wall-tangential components show nearly unchanged distributions in the zero pressure gradient region and a slight increase in the wave trough in the adverse pressure gradient region.

6 Conclusion

Spanwise traveling transversal surface waves were applied to a wing section with a DRA2303 geometry in a turbulent flow. The purpose of this investigation was to prove that in engineering-like flow scenarios with favorable, zero, and adverse pressure gradients and non-zero surface curvature drag reduction can be achieved.

The turbulent flow was simulated by a high-resolution implicit LES. The boundary layer was tripped near the leading edge. About 74% of the surface underwent a transversal spanwise wave motion with a variation of the amplitude in the streamwise direction.

A reduction of the integrated total drag by 7.5% is obtained and the lift coefficient is enlarged by 1.4%. The simultaneous improvement of both coefficients is due to the reduction of the streamwise turbulence intensities and a decreased boundary-layer thickness. This is in contrast to findings of the technique of blowing into the turbulent boundary layer, where the turbulence production is primarily shifted off the wall, leading to a thickened boundary layer and an increased pressure drag [4]. The main reason for the drag reduction is the significantly lowered wall-normal vorticity fluctuations.

References

1. M. Albers, P.S. Meysonnat, W. Schröder, Drag reduction via transversal wave motions of structured surfaces, in *International Symposium on Turbulence & Shear Flow Phenomena (TSFP-10)* (2017)
2. M. Albers, P.S. Meysonnat, W. Schröder, Actively reduced airfoil drag by transversal surface waves. *Flow Turbul. Combust.* **102**(4), 865–886 (2019)
3. P.H. Alfredsson, R. Örlü, Large-eddy breakup devices - a 40 years perspective from a Stockholm horizon. *Flow Turbul. Combust.* **100**(4), 877–888 (2018)
4. M. Atzori, R. Vinuesa, A. Stroh, B. Frohnäpfel, P. Schlatter, Assessment of skin-friction-reduction techniques on a turbulent wing section, in *12th ERCOFTAC Symposium on Engineering Turbulence Modeling and Measurements (ETMM12)* (2018)
5. H.L. Bai, Y. Zhou, W.G. Zhang, S.J. Xu, Y. Wang, R.A. Antonia, Active control of a turbulent boundary layer based on local surface perturbation. *J. Fluid Mech.* **750**, 316 (2014)
6. D.W. Bechert, G. Hoppe, W.E. Reif, On the drag reduction of the shark skin, in *AIAA Paper No. 85-0546* (1985)
7. D. Bechert, R. Meyer, W. Hage, Drag reduction of airfoils with miniflaps - can we learn from dragonflies? in *AIAA Paper No. 2000-2315* (2000)
8. J.P. Boris, F.F. Grinstein, E.S. Oran, R.L. Kolbe, New insights into large eddy simulation. *Fluid Dyn. Res.* **10**(4–6), 199–228 (1992)
9. S.L. Ceccio, Friction drag reduction of external flows with bubble and gas injection. *Annu. Rev. Fluid Mech.* **42**(1), 183–203 (2010)
10. K.S. Choi, X. Yang, B.R. Clayton, E.J. Glover, M. Atlar, B.N. Semenov, V.M. Kulik, Turbulent drag reduction using compliant surfaces. *Proc. R. Soc. Lond. Ser. A* **453**(1965), 2229–2240 (1997)
11. Y. Du, G.E. Karniadakis, Suppressing wall turbulence by means of a transverse traveling wave. *Science* **288**(5469), 1230–1234 (2000)

12. Y. Du, V. Symeonidis, G.E. Karniadakis, Drag reduction in wall-bounded turbulence via a transverse travelling wave. *J. Fluid Mech.* **457**, 1–34 (2002)
13. A. Feldhusen-Hoffmann, V. Statnikov, M. Klaas, W. Schröder, Investigation of shock-acoustic-wave interaction in transonic flow. *Exp. Fluids* **59**(1), 15 (2017)
14. J.L. Fulker, M.J. Simmons, *An Experimental Investigation of Passive Shock/Boundary-Layer Control on an Aerofoil* (Vieweg+Teubner Verlag, Wiesbaden, 1997), pp. 379–400
15. M. Gad-el-Hak, *Flow Control : Passive, Active, and Reactive Flow Management* (Cambridge University Press, Cambridge, 2000)
16. R. García-Mayoral, J. Jiménez, Hydrodynamic stability and breakdown of the viscous regime over riblets. *J. Fluid Mech.* **678**, 317–347 (2011)
17. G. Geiser, *Thermoacoustic Noise Sources in Premixed Combustion* (Verlag Dr. Hut, München, 2014)
18. J.W. Gose, K. Golovin, M. Boban, J.M. Mabry, A. Tuteja, M. Perlin, S.L. Ceccio, Characterization of superhydrophobic surfaces for drag reduction in turbulent flow. *J. Fluid Mech.* **845**, 560–580 (2018)
19. R. Henke, “A320 HLF Fin” flight tests completed. *Air & Space Eur.* **1**(2), 76–79 (1999)
20. C.W. Hirt, A.A. Amsden, J.L. Cook, An arbitrary Lagrangian-Eulerian computing method for all flow speeds. *J. Comput. Phys.* **14**, 227–253 (1974)
21. S.M. Hosseini, R. Vinuesa, P. Schlatter, A. Hanifi, D.S. Henningson, Direct numerical simulation of the flow around a wing section at moderate Reynolds number. *Int. J. Heat Fluid Flow* **61**, 117–128 (2016)
22. M. Itoh, S. Tamano, K. Yokota, S. Taniguchi, Drag reduction in a turbulent boundary layer on a flexible sheet undergoing a spanwise traveling wave motion. *J. Turbul.* **7**, N27 (2006)
23. J. Jeong, F. Hussain, On the identification of a vortex. *J. Fluid Mech.* **285**, 69–94 (1995)
24. J. Jiménez, Turbulent flows over rough walls. *Annu. Rev. Fluid Mech.* **36**(1), 173–196 (2004)
25. J. Jiménez, A. Pinelli, The autonomous cycle of near-wall turbulence. *J. Fluid Mech.* **389**, 335–359 (1999)
26. W.J. Jung, N. Mangiavacchi, R. Akhavan, Suppression of turbulence in wall bounded flows by high frequency spanwise oscillations. *Phys. Fluids A* **4**(8), 1605–1607 (1992)
27. Y. Kametani, K. Fukagata, R. Örlü, P. Schlatter, Effect of uniform blowing/suction in a turbulent boundary layer at moderate Reynolds number. *Int. J. Heat Fluid Flow* **55**, 132–142 (2015)
28. E. Kim, H. Choi, Space-time characteristics of a compliant wall in a turbulent channel flow. *J. Fluid Mech.* **756**, 30–53 (2014)
29. S. Klumpp, M. Meinke, W. Schröder, Numerical simulation of riblet controlled spatial transition in a zero-pressure-gradient boundary layer. *Flow Turbul. Combust.* **85**(1), 57–71 (2010)
30. S. Klumpp, M. Meinke, W. Schröder, Drag reduction by spanwise transversal surface waves. *J. Turbul.* **11** (2010)
31. S.R. Koh, P. Meysonnat, V. Statnikov, M. Meinke, W. Schröder, Dependence of turbulent wall-shear stress on the amplitude of spanwise transversal surface waves. *Comput. Fluids* **119**, 261–275 (2015)
32. M.S. Liou, C. Steffen, A new flux splitting scheme. *J. Comput. Phys.* **107**, 23–39 (1993)
33. P.Q. Liu, H.S. Duan, J.Z. Chen, Y.W. He, Numerical study of suction-blowing flow control technology for an airfoil. *J. Aircr.* **47**(1), 229–239 (2010)
34. M. Luhar, A. Sharma, B. McKeon, A framework for studying the effect of compliant surfaces on wall turbulence. *J. Fluid Mech.* **768**, 415–441 (2015)
35. M. Meinke, W. Schröder, E. Krause, T. Rister, A comparison of second- and sixth-order methods for large-eddy simulations. *Comput. Fluids* **31**(4), 695–718 (2002)
36. P.S. Meysonnat, S.R. Koh, B. Roidl, W. Schröder, Impact of transversal traveling surface waves in a non-zero pressure gradient turbulent boundary layer flow. *Appl. Math. Comput.* **272**, 498–507 (2016)
37. P.S. Meysonnat, D. Roggenkamp, W. Li, B. Roidl, W. Schröder, Experimental and numerical investigation of transversal traveling surface waves for drag reduction. *Eur. J. Mech. B. Fluids* **55**, 313–323 (2016)

38. P. Moin, T. Shih, D. Driver, N.N. Mansour, Direct numerical simulation of a three dimensional turbulent boundary layer. *Phys. Fluids A* **2**(10), 1846–1853 (1990)
39. R. Nakanishi, H. Mamori, K. Fukagata, Relaminarization of turbulent channel flow using traveling wave-like wall deformation. *Int. J. Heat Fluid Flow* **35**, 152–159 (2012)
40. M. Perlin, D.R. Dowling, S.L. Ceccio, Freeman scholar review: passive and active skin-friction drag reduction in turbulent boundary layers. *J. Fluids Eng.* **138**(9), 091104–091116 (2016)
41. M. Quadrio, Drag reduction in turbulent boundary layers by in-plane wall motion. *Philos. Trans. R. Soc. Lond. Ser. A* **369**(1940), 1428–1442 (2011)
42. M. Quadrio, P. Ricco, C. Viotti, Streamwise-travelling waves of spanwise wall velocity for turbulent drag reduction. *J. Fluid Mech.* **627**, 161 (2009)
43. J. Reneaux, Overview on drag reduction technologies for civil transport aircraft, in *European Congress on Computational Methods in Applied Sciences and Engineering (ECCOMAS)* (2004)
44. B. Roidl, M. Meinke, W. Schröder, Zonal RANS-LES computation of transonic airfoil flow, in *AIAA Paper No. 2011–3974* (2011)
45. P. Schlatter, R. Örlü, Turbulent boundary layers at moderate Reynolds numbers: inflow length and tripping effects. *J. Fluid Mech.* **710**, 5–34 (2012)
46. H. Shan, L. Jiang, C. Liu, Direct numerical simulation of flow separation around a NACA 0012 airfoil. *Comput. Fluids* **34**(9), 1096–1114 (2005)
47. P.R. Spalart, J.D. McLean, Drag reduction: enticing turbulence, and then an industry. *Philos. Trans. R. Soc. Lond. Ser. A* **369**(1940), 1556–1569 (2011)
48. E. Stanewsky, J. Détery, J. Fulker, P. de Matteis, Synopsis of the project EUROSHOCK II, in *Drag Reduction by Shock and Boundary Layer Control*, ed. by E. Stanewsky, J. Détery, J. Fulker, P. de Matteis (Springer, Berlin, 2002), pp. 1–124
49. J. Szodrach, Viscous drag reduction on transport aircraft, in *AIAA Paper No. 91–0685* (1991)
50. S. Tamano, M. Itoh, Drag reduction in turbulent boundary layers by spanwise traveling waves with wall deformation. *J. Turbul.* **13**, N9 (2012)
51. N. Tomiyama, K. Fukagata, Direct numerical simulation of drag reduction in a turbulent channel flow using spanwise traveling wave-like wall deformation. *Phys. Fluids* **25**(10), 105115 (2013)
52. R. Vinuesa, P. Schlatter, Skin-friction control of the flow around a wing section through uniform blowing, in *European Drag Reduction and Flow Control Meeting (EDRFCM 2017)* (2017)
53. R. Vinuesa, C. Prus, P. Schlatter, H.M. Nagib, Convergence of numerical simulations of turbulent wall-bounded flows and mean cross-flow structure of rectangular ducts. *Meccanica* **51**(12), 3025–3042 (2016)
54. R. Vinuesa, P.S. Negi, M. Atzori, A. Hanifi, D.S. Henningson, P. Schlatter, Turbulent boundary layers around wing sections up to $Re_c = 1,000,000$. *Int. J. Heat Fluid Flow* **72**, 86–99 (2018)
55. M. Walsh, L. Weinstein, Drag and heat transfer on surfaces with small longitudinal fins, in *11th Fluid and Plasma Dynamics Conference* (1978), p. 1161
56. C. Zhang, J. Wang, W. Blake, J. Katz, Deformation of a compliant wall in a turbulent channel flow. *J. Fluid Mech.* **823**, 345–390 (2017)
57. H. Zhao, J.Z. Wu, J.S. Luo, Turbulent drag reduction by traveling wave of flexible wall. *Fluid Dyn. Res.* **34**(3), 175–198 (2004)